


Article

# Influence of Flanks on Resistance Performance of High-Speed Amphibious Vehicle

Dibo Pan, Xiaojun Xu \* and Bolong Liu 

College of Intelligence Science and Technology, National University of Defense Technology, Changsha 410073, China; pandibo19@nudt.edu.cn (D.P.); liubolong15@nudt.edu.cn (B.L.)

\* Correspondence: xiaojunxu@nudt.edu.cn

**Abstract:** In order to reduce the additional resistance of high-speed amphibious vehicles, Flanks are designed on the concave grooves. As a new drag reduction attachment, the principle of Flanks is analyzed and discussed in detail. In this paper, the HSAV model and Flanks coupling resistance tests are performed based on the Reynolds-averaged Navier–Stokes method and SST  $k - \omega$  model. The accuracy of the numerical approach is verified by a series of towing tests. Results show that with a fixed installation angle and invariable characteristic parameters, Flanks can significantly reduce the total resistance at high speed, with a maximum drag reduction of 16%. In the meantime, Flanks also affect the attitude and flow field of the vehicle, consequently affecting the resistance composition and the sailing condition. A vehicle model self-propulsion test is designed and carried out, and it qualitatively verifies the drag reduction effect of the Flanks at high speed.

**Keywords:** amphibious vehicle; resistance performance; CFD; towing test; hydrodynamic characteristics



**Citation:** Pan, D.; Xu, X.; Liu, B. Influence of Flanks on Resistance Performance of High-Speed Amphibious Vehicle. *J. Mar. Sci. Eng.* **2021**, *9*, 1260. <https://doi.org/10.3390/jmse9111260>

Academic Editor: Alessandro Ridolfi

Received: 23 October 2021  
Accepted: 10 November 2021  
Published: 12 November 2021

**Publisher's Note:** MDPI stays neutral with regard to jurisdictional claims in published maps and institutional affiliations.



**Copyright:** © 2021 by the authors. Licensee MDPI, Basel, Switzerland. This article is an open access article distributed under the terms and conditions of the Creative Commons Attribution (CC BY) license (<https://creativecommons.org/licenses/by/4.0/>).

## 1. Introduction

Cruising speed, which plays a crucial role in battlefield survivability of high-speed amphibious vehicles (HSAVs), is one of the most important indicators. HSAVs are equipped with wheels, tracks, or other mechanisms to maintain their walking ability on land [1]. The hull geometry of amphibious vehicles differs significantly from ships, such as smaller aspect ratios, more rapid changes in section shape, blunter bows, etc. [2,3]. Therefore, the water resistance of a HSAV is larger than that of the ship, resulting in slower speed [1–3].

Water resistance of a HSAV includes friction resistance, viscous pressure resistance, and wave-making resistance. Duan et al. showed that the friction resistance is relatively small; the viscous pressure and wave-making resistance occupy the main parts [2]. Friction resistance accounts for only 8–10% of the total resistance, while 40–80% of the viscous pressure resistance. Wave-making resistance is closely associated with speed, and it accounts for 15–20% of the total force when sailing from 9 to 11 km/h. Additionally, the higher the speed is, the greater the proportion is. Ehrlich et al. fitted the relations between drag characteristics and speed and discussed the impact of three drag components, respectively [4]. Results pointed out that the friction and viscous pressure resistance are proportional to the 1.8th power of velocity, while wave-making resistance to the 4th approximately. Some scholars continued this analysis method [5,6]. All research above indicates that reducing viscous pressure resistance and wave-making resistance can effectively improve the drag characteristics of HSAVs.

Essentially, the viscous pressure resistance and wave-making resistance of a HSAV are changed dramatically due to its particular configuration. Relevant studies illustrated that the walking mechanism destroys the hull's coherence, leading to increased viscous pressure resistance [2,3,7–10]. In addition, features such as small aspect ratio  $L/B$ , small draft ratio  $B/T$ , and blunt bows strengthen the viscous pressure resistance and increase the bow wave. Therefore, redesigning the surface and adding attachments are effective methods of drag reduction.

According to the open literature, little research has been designed to study the drag reduction of HSAVs. Lee et al. installed a hydrofoil in the craft's bow [7], which can successfully improve bow trim at high Froude number ( $Fr$ ). Latorre and Arana agreed with this conclusion [3]. They compared HSAV resistance with and without a bow hydrofoil at different  $Fr$ , showing that the bow hydrofoil can cut down the total resistance by more than 10% when  $Fr$  exceeds 0.25. Moreover, the drag reduction percentage can reach 17% when  $Fr$  equals 0.3. Helvacioğlu et al. studied the cruising ability of HSAVs [11]. Ain et al. analyzed the influence of an air cushion on the resistance of a Multi Amphibious Vehicle [9]. Results confirm that the air cushion effect is helpful to depress drag, but it weakens with the increase of speed and wave height. Moreover, the air injection devices will increase weight and draft, negatively affecting the vehicle's resistance to wind and waves. Sun et al. studied the effect of stern flaps on a caterpillar track amphibious vehicle (CTAV), which will perform better by improving trim, lessening draft, and increasing virtual length [12]. When  $Fr$  is between 0.63 and 1.05, the drag reduction impact can reach 34.31%. Additionally, the optimal angle of Stern Flaps varies with different speeds.

Even though there are so many measures to reduce the resistance, few can be applied to HSAVs. With speed increase, the cruising state gradually changes from floating to planning, which means the hydrodynamic lift will exceed the buoyancy [8]. In the meantime, the waterline moves down, and the bow will be carried out of water. Therefore, the wave will focus on the front concave groove, significantly affecting the viscous pressure and wave-making resistance. In conclusion, drag reduction methods on the front concave groove will be effective.

Resistance extrapolation methods widely used include data-based estimation, semi-empirical, resistance chart, towing test, and numerical approach [13]. The data-based estimation method is efficient and straightforward, but the accuracy is poor and the data on amphibious vehicles are scarce. The semi-empirical method combines a theoretical formula with experimental correction to reflect the objective law. However, the structure of HSAVs is quite different from conventional crafts, and also the resistance characteristics [8]. The resistance chart method requires high shape consistency, so it is unable to be applied to HSAVs. The towing test method and numerical approach all have high accuracy and realizability [14,15], and their combination can effectively evaluate the HSAV's resistance.

In this study, the influence of Flanks on a HSAV's resistance is illustrated. To restrain the sharp increase of pressure resistance and wave-making resistance at high speed, a new attachment is designed and installed at the front concave groove. According to the classification of resistance, the drag reduction theory is expounded. Numerical method and Towing test are applied to analyze the force condition without and with Flanks. The effect of Flanks on resistance is verified by analyzing a HSAV's sailing attitude. Last, a self-propulsion model experiment is designed to verify the effect of Flanks under natural conditions qualitatively.

## 2. Resistance Analysis

The hull geometry of a HSAV has a significant influence on the resistance [1–3]. Consequently, the Flanks concept is proposed as a significant innovation. The uppercase "Flanks" mentioned in this paper refers to the drainage plate located at the concave groove. The shape and installation location can be seen in Figures 1 and 2. Flanks can avoid vortices at the concave groove by steering the water flow. It also alleviates the stress concentration and lowers the water surface in grooves. Based on unaltered laminar flow, this construction can minimize energy loss and maintain fluid velocity.

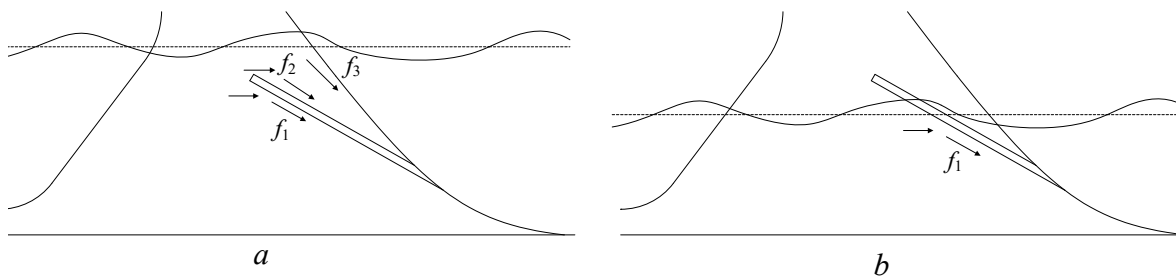


**Figure 1.** Diagram of friction at Flanks and concave groove. (a) Flanks are underwater; (b) Flanks expose the free surface.

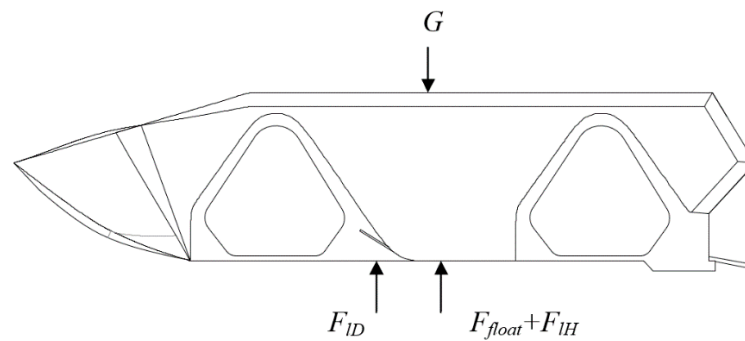


**Figure 2.** Equilibrium relation of HSAV weight.

### 2.1. Friction Resistance

Friction resistance is calculated according to Froude Postulates. It is believed that HSAV friction resistance is equal to that of a flat plate with the same speed, length, and wetted surface. Friction resistance can be described by the non-dimensional number  $C_f$ :

$$R_f = C_f \cdot \left( \frac{1}{2} \rho v^2 S \right) \tag{1}$$

where  $\rho$  is the density of water,  $v$  is the cruising speed of the vehicle,  $S$  is the wetted surface.

$C_f$  can be obtained as  $C_f = 0.075 / (\lg Re - 2)^2$ , and it is exclusively related to the Reynolds number. When the overall configuration of the vehicle is unchanged,  $C_f$  remains constant at the same speed. Therefore,  $R_f$  is proportional to the wetted surface  $S$ .

There are two ways to change the friction force. One is shown in Figure 1 when Flanks are underwater (Figure 1a), friction increases by adding  $f_1$  and  $f_2$  compared with the original hull ( $f_3$ ). Furthermore, only  $f_1$  will exist when Flanks expose the free surface (Figure 1b). The second is to change the wet surface by adding lift force  $F_{ID}$  on Flanks, as shown in Figure 2. The buoyancy force  $F_{float}$  will decrease with the addition of  $F_{ID}$ , resulting in the reduction of wetted surfaces.

### 2.2. Viscous Pressure Resistance

Viscous pressure resistance is caused by the pressure difference. Figure 3 shows the cause of viscous pressure resistance. When water particles move from the front stagnation point A to the rear, their velocity increases first and then decreases. Their kinetic energy runs out at point D, resulting in a pressure drop in the rear. The pressure difference between the front and the rear of the vehicle leads to viscous pressure resistance [13].

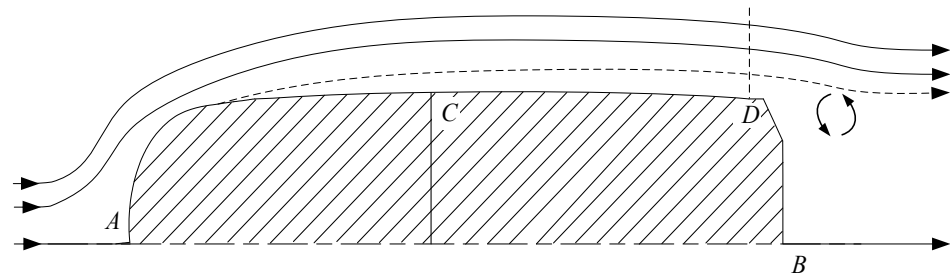


Figure 3. Diagram of HSAV streamline.

Obviously, to lower the viscous pressure resistance of HSAVs, measures should be taken to reduce the kinetic energy loss. Flanks can reduce the kinetic energy loss when water impacts the vehicle surface. As shown in Figure 4, when the water stream enters the inclined plane at an angle, part of the kinetic energy is dissipated by vortices on the upper side of the impact point. After the installation of Flanks, the inflow angle is improved, as well as the energy loss.

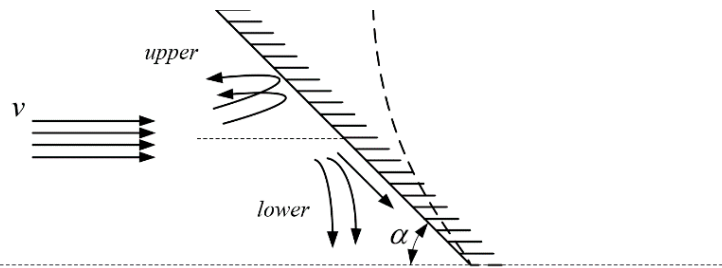


Figure 4. Diagram of water particle impact plate.

### 2.3. Wave Making Resistance

When sailing at high speed, the percentage of wave-making resistance increases significantly. With the increase of bow trim, the front concave groove becomes the new ‘bow’ and dramatically influences wave-making resistance.

The wave is formatted by uneven distribution of pressure, which leads to height fluctuation of water around the hull, resulting in wave-making resistance. According to the assumption of the plane traveling wave, the wave-making resistance  $R_w$  can be described as:

$$R_w = \frac{1}{4} \rho g A^2 b \tag{2}$$

where  $A$  is wave amplitude. Assuming that the water moves from infinite distance point  $a$  to point  $b$ , the wave amplitude  $A_b$  in point B is:

$$A_b \propto Z_b = \frac{v_a^2 - v_b^2}{2g} \tag{3}$$

From the Equations (2) and (3), with the increase of  $v_b$ , the wave-making resistance  $R_w$  will decline. Therefore, alleviating the velocity loss of water at grooves is an effective measure to reduce wave-making resistance.

### 2.4. Double Body Test

The double body test is applied to solve the resistance components. HSAVs travel at the interface between air and water, where the wave is created. When viscous pressure resistance is calculated only, the influence of wave should be left out. The water surface can be regarded as a symmetry plane, and the part below is mirrored [16].

Based on the three-dimensional extrapolation proposed by Hughes [17], friction and viscous pressure resistance are related to the viscosity Reynolds number. They are

collectively called the viscous resistance  $C_v$  ( $C_v = (1 + k)C_f$ ),  $k$  is the shape coefficient. Therefore, total drag coefficient in the free liquid model can be described as:

$$C_t = (1 + k)C_f + C_w \tag{4}$$

In the double body model, wave-making resistance coefficient  $C_{w'} = 0$ , the total resistance coefficient  $C_{t'}$  is:

$$C_{t'} = (1 + k')C_{f'} \tag{5}$$

where  $C_f$  and  $C_{f'}$  are the friction coefficients of the free liquid model and double-body. The shape factors of HSAVs can be considered to be equal, that is:

$$(1 + k) = (1 + k') \tag{6}$$

Then, the wave-making resistance is the difference of total resistance between the free liquid model and double body test [18,19].

$$C_w = C_t - C_{t'} \tag{7}$$

By calculating Equations (4)–(7), the friction resistance, viscous pressure resistance, and wave-making resistance of HSAVs at different velocities can be obtained accurately.

### 3. Numerical Simulation

Computational fluid dynamics (CFD) is an essential method for analyzing hydrodynamics, flow field characteristics, and scale effects of crafts [20]. In this study, the results of numerical simulation and towing test were compared to verify the accuracy of CFD. The resistance, trim, and sinkage were used to evaluate the effect of Flanks. By using the double-body method, the resistance component of the HSAV was obtained. All of them were based on STAR-CCM+ software provided by CD-Adapco, New York, USA.

#### 3.1. Geometric Model

The 1:1 model of the HSAV was used for simulation, which was 5.702 m in length and 2.151 m wide. The model was a triangular tracked vehicle with tail flaps and a sleek design in the bow. When sailing on the water, the HSAV was propelled by a jet pump. The vehicle model was simplified to facilitate the numerical calculation and towing test, the track wheel was closed, and the sensor on the upper surface was removed. The hull geometry is shown in Figure 5, and main parameters are shown in Table 1.

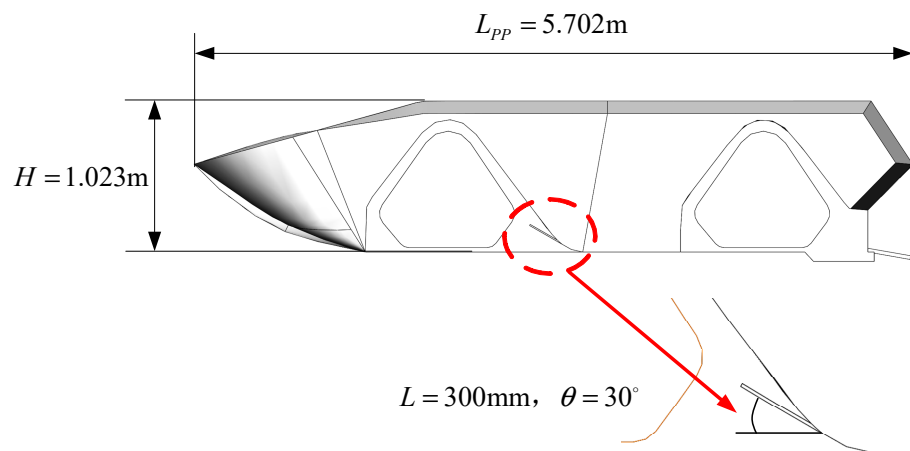


Figure 5. Geometric model of HSAV.

**Table 1.** Main geometric parameters of the vehicle model.

Items	Symbol	Value
Scale ratio	$\lambda$	1
Model length	$L_{pp}$ (m)	5.702
Modeled breadth	$B$ (m)	2.151
Modeled height	$H$ (m)	1.203
Draught	$D$ (m)	0.378
Wetted surface	$S$ (m <sup>2</sup> )	15.717
Volume	$\nabla$ (m <sup>3</sup> )	3.169
Length of Flanks	$l$ (mm)	300
Breadth of Flanks	$b$ (mm)	305
Install angle	$\theta$ (deg)	30

### 3.2. Governing Equations and Turbulence Model

The numerical solution of the flow field was obtained by the CFD method based on the fluid’s generalized continuity equation and momentum equation. The equations were solved based on the three-dimensional incompressible implicit unsteady model, Reynolds average Navier–Stokes equation [21,22], and turbulence model [23].

The selection of turbulence model is the premise of an accurate solution. Wan et al. compared various turbulence models’ accuracies in solving amphibious vehicles’ flow fields [24]. Results are shown in Table 2.

**Table 2.** Comparison of different turbulence models.

Turbulence Model	S-A [25]	Standard Model $k-\epsilon$ [26,27]	RNG $k-\epsilon$ [28]	Realizable $k-\epsilon$ [29]	Standard Model $k-\omega$ [24]	SST $k-\omega$ [30]
Solution error	1.58%	15.2%	8.51%	1.19%	20.6%	0.791%

Therefore, the shear-stress transport (SST)  $k-\omega$  turbulence model was selected to simulate the strong adverse pressure gradient flow field.

Equation  $k$ :

$$\rho \frac{\partial}{\partial x_i} (ku_i) = \frac{\partial}{\partial x_i} \left( \Gamma_k \frac{\partial k}{\partial x_i} \right) + G_k - \rho \beta^* k \omega \tag{8}$$

Equation  $\omega$ :

$$\rho \frac{\partial}{\partial x_i} (\epsilon u_i) = \frac{\partial}{\partial x_i} \left( \Gamma_\omega \frac{\partial \epsilon}{\partial x_i} \right) + \alpha \frac{\omega}{k} G_k - \rho \beta_i \omega^2 + 2(1 - F) \rho \sigma_{\omega 2} \frac{1}{\omega} \frac{\partial k}{\partial x_i} \frac{\partial \omega}{\partial x_i} \tag{9}$$

where  $\beta^* = 0.09$ ,  $\alpha = 0.52$ ,  $\beta_i = 0.072$ ,  $\sigma_\omega = 2.0$ ,  $\sigma_{\omega 2} = 1.168$ . The mathematical formula of other turbulence models mentioned can be found in [25,28–31].

The VOF model was applied to deal with the free surface between air and water [32,33]. Moreover, the dynamic fluid–body interaction (DFBI) model was used to control the vehicle’s attitude.

### 3.3. Mesh and Domain

The model calculation domain is shown in Figure 6. According to the guidance of ITTC [34], the orthogonal calculation domain of  $5L_{pp} \times 3L_{pp} \times 2L_{pp}$  was established, where  $L_{pp}$  is the length between the head and tail of the vehicle model [12].

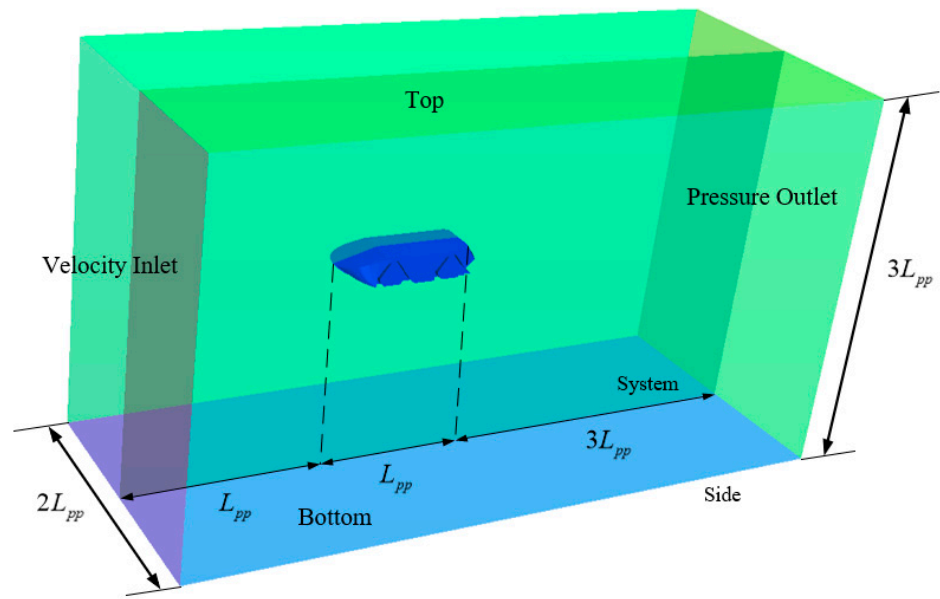


Figure 6. Computational domain.

The boundary condition of the inlet was set as velocity-inlet, and the inflow speed was the cruising velocity in the simulation. The pressure-outlet was applied to the outlet of the domain. In order to simplify the calculation, only half of the model was calculated. The symmetry condition was applied to the symmetry plane and side plane of the domain. The top and bottom were also set as velocity-inlet. The hull was defined as a non-slip surface; the air and water phases were set and defined by the VOF model [20].

The meshing quality will influence the convergence index and correction factor, further affecting the quantitative estimation of the time step uncertainty [35]. The overset grid method was used to divide the mesh [36], as shown in Figure 7a. Figure 7b shows the Kelvin wave refinement area used to capture the traveling waves. The refinement approach for Flanks is shown in Figure 7c. Figure 7d shows the mesh near the vehicle, and the area was refined to ensure calculation accuracy. The wall function method was used to deal with the flow near the wall, and the dimensionless number  $y^+$  was controlled between 30 and 300 to meet the requirement [37].

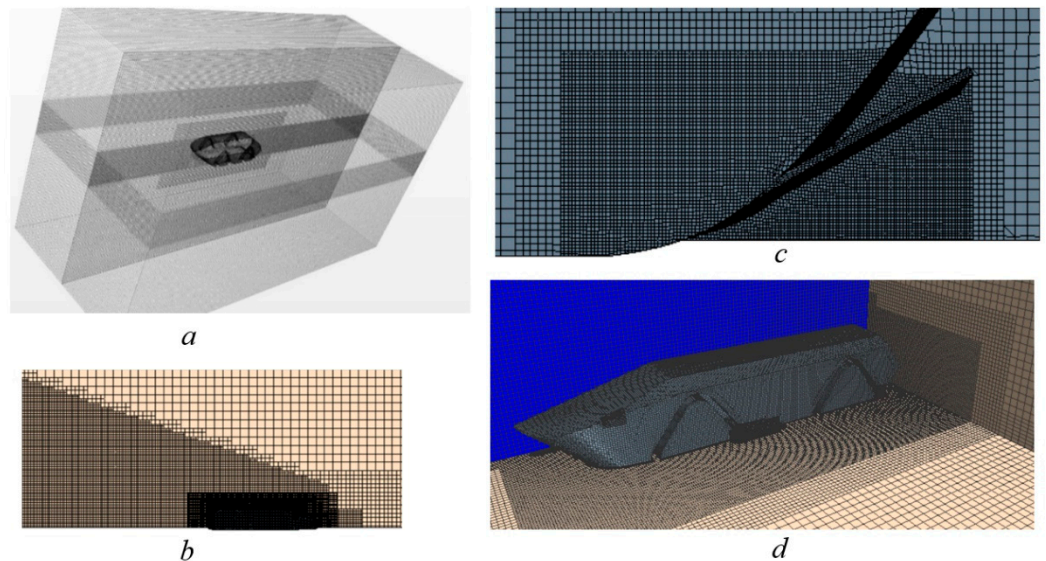


Figure 7. Diagram of mesh. (a) Overall mesh; (b) Kelvin wave system; (c) Encryption area of Flanks; (d) Mesh of the hull.

A variety of refinement parameters are used to study the convergence and independence of grid parameters [35,38]. Three grid parameters were selected according to ITTC recommendation [38], which are Grid-1 with coarse grids, Grid-2 with intermediate grids, and Grid-3 with fine grids. By reference to the result of EFD (scale ratio  $\lambda = 2.5$ ), these three types of grids were calculated and compared in  $Fr = 0.89$ . The results of the grid independence test are shown in Table 3 (on the model scale).

It can be seen that the convergence ratio (described in [39]) of the resistance is below 1, thereby demonstrating the monotonic convergence of the grids. The errors are all less than 5%. With the careful consideration of scale ratio, simulation time cost, and result accuracy, Grid-2 (Middle grids) was selected for simulation.

**Table 3.** Resistance calculation results under different mesh conditions.

Type	Grid Size	CPU Time	$R_t$ (N) (Model Scale)	Error (%)
EFD	-	-	527.56928	-
Grid-1	664,870	44.6 s	550.61593	4.368%
Grid-2	1,892,774	111.21 s	533.02555	1.034%
Grid-3	5,335,595	283.5 s	525.98311	-0.301%

## 4. Results and Discussions

### 4.1. Verification of CFD

The author's team conducted the towing tests in a high-speed hydrodynamic laboratory in Jingmen, Hubei Province. The laboratory pool was 510 m long, 6.5 m wide, and 6.8 m deep. The experimental depth of water was 5 m, and the water temperature was 20 °C. The control precision of speed in the towing experiment was better than 0.2%.

The picture of towing test is shown in Figure 8. The model was designed according to the scale of 1:2.5 of the original vehicle, made of solid wood and shaped by a five-axis machine tool. The cavity of the lifting mechanism was filled to facilitate the processing. The CFD model used for verification was also filled relatively. The surface of the model was waterproof and spray-painted, which meets the standard of ITTC. A towing device was installed at the gravity center of the model, with a trailer system to provide power and stable speed. The resistance sensor was connected to the drag point by wire rope. The trim and heave were free and could be measured by the inclination sensor and position sensor. The parameters of these instruments are shown in Table 4.

The parameters of model ship are shown in Table 5. The reference frame was located at the intersection of the middle section of two front wheels and the middle axis at the bottom, and the  $x$ -axis points to the rear.



**Figure 8.** Picture of towing test.



**Table 4.** Parameters of towing test instruments.

Instrument	Type	Measuring Range	Precision
Data acquisition system	PXI-EQ1230	±10 VDC	16 bit 0.3%
Resistance sensor	U3B1-100K-B	±200 kg	0.01 kg
Inclination sensor	ACCUSTAR	±60°	0.01°
Position sensor	CLMD2-AJB8P011000	1.0 m	0.01 mm

**Table 5.** Parameters of the model ship.

Items	Value	Items	Value
Weight	192 kg	Scale ratio	1:2.5
Longitudinal coordinates of the gravity center	540 mm	Initial bow draft	93 mm
Vertical coordinates of the gravity center	200 mm	Initial stern draft	140 mm

In calm water, tests were completed at five speeds from 1 to 5 m/s. During the experiments, the speed and resistance of the vehicle were recorded. The data collected by the experiment method (hereafter called EFD) were compared with the results of CFD to verify the accuracy of the numerical model.

The results of CFD and EFD are compared in Figure 9, which shows good consistency. Resistances of CFD were converted to the scale of the towing test. As shown in Figure 9a, the overall resistance error between CFD and EFD is only 3.18%. Considering the scale effect and the error caused by the simulation model, an error below 5% is generally considered acceptable [39–41]. Results of trim show good consistency, the average error is 5.95%, and the maximum value error of 7.67% occurs at  $Fr = 0.89$ . The trim error is more significant than resistance at high speed due to the large impact moment on the model caused by high-speed flow and large trim angle. By reference to [39], the reliability and accuracy of the simulation model were effectively verified.

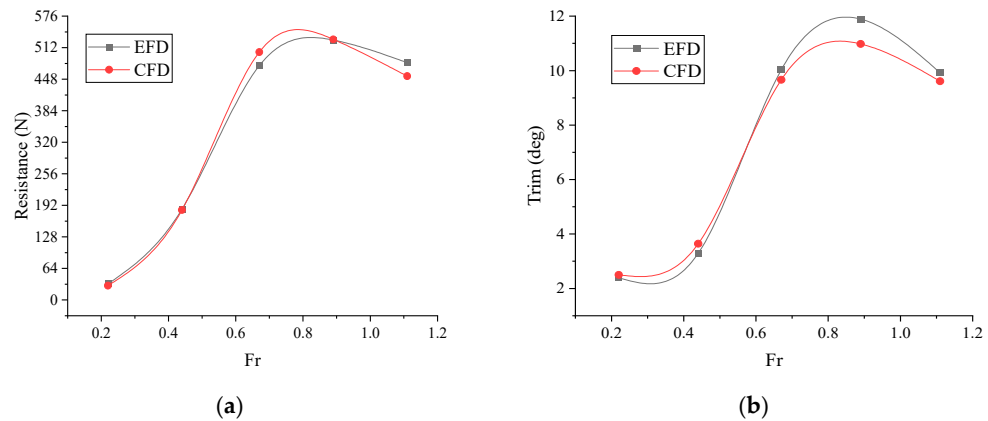


**Figure 9.** Comparison of results between EFD and CFD. (a) Resistance; (b) Trim.

Figure 10 shows the free liquid surface waveforms of the towing test and CFD simulation in  $Fr = 0.67$ . It shows that the phenomena are highly consistent in front wave (1), rear “cocktail” (2), and rear “Kelvin wave” (3), as well as the draught (heave) and trim. Therefore, the numerical calculation method has high accuracy and credibility, which can support the following analysis.

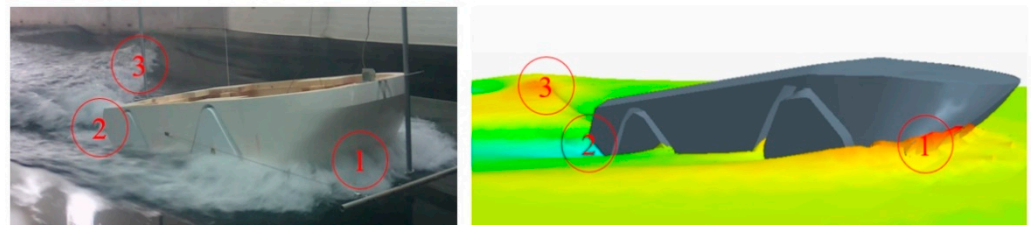


Figure 10. Comparison of the surface wave between EFD and CFD.

4.2. Influence on Total Resistance

The total resistance and drag reduction rate  $\eta_t$  of the HSAV without and with Flanks were compared. Flanks are always fixed at an angle of  $30^\circ$  with the bottom surface. Expressions of drag reduction rate  $\eta_t$  and Froude number  $Fr$  are as follows:

$$\eta_t = (R_{t0} - R_{t1}) / R_{t0} \tag{10}$$

$$Fr = v / \sqrt{gL} \tag{11}$$

where  $R_t$  is the total resistance, the subscripts 0 and 1 are adopted to represent the original vehicle and vehicle with Flanks.  $v$  is the cruising speed of the HSAV.  $L$  means the length of the waterline. Flanks are expected to play a strong drag reduction effect at medium and high speed, as shown by Figure 11.

- (1) When  $Fr > 0.86$ , Flanks begin to play a drag reduction effect. The maximum drag reduction effect occurs in  $Fr = 1.23$ , which is expected to achieve 16.0%.
- (2) When  $Fr < 0.86$ , there is no drag reduction effect due to low velocity. Combined with the analysis in Section 2, Flanks at low speed will cause an increase in resistance. The influence of trim and sinkage on resistance will be studied next.

Therefore, Flanks should be folded at low speed and unfolded when the speed reaches a higher stage. Additionally, angles of Flanks in different cruising attitudes ought to be analyzed in detail. In this paper, comparison and optimization of multi-parameters are not involved. The Flanks with only one angle and length were analyzed to clarify their drag reduction principle and effectiveness in more detail.

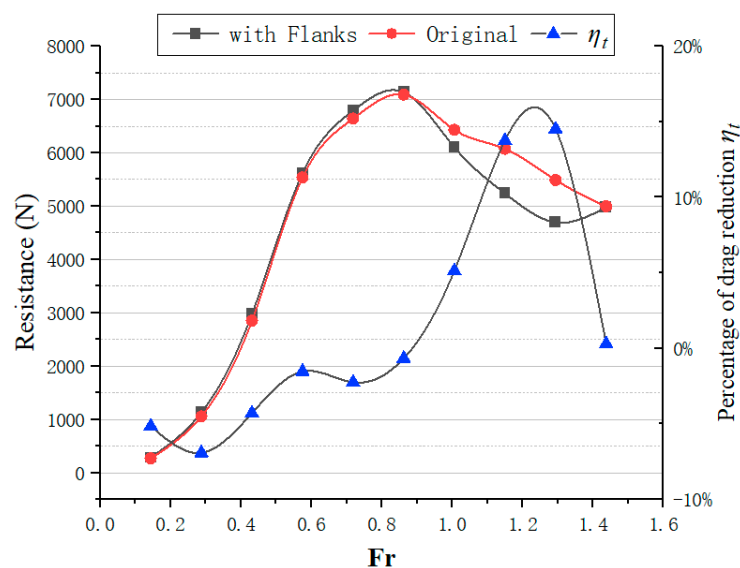


Figure 11. Comparison and drag reduction effect of the two schemes.

The dynamic resistance ratio  $r_{D/t}$  is used to describe the resistance ratio of Flanks. Based on  $r_{D/t}$ , the potential of drag reduction at different speeds could be seen. Expression of  $r_{D/t}$  is shown as follows:

$$r_{D/t} = R_D / R_t \tag{12}$$

where  $R_D$  is the resistance of Flanks, which can be measured directly by extracting the surface as a separate boundary in CFD software (STAR-CCM+ software provided by CD-Adapco, New York, USA).

In Figure 12, with the improvement of speed, the total resistance of the whole vehicle increases at first and then decreases, and it reaches the peak at  $Fr = 0.86$ . The resistance peak is the threshold for the transition of the HSAV from floatation state dominated by buoyancy to planing state dominated by hydrodynamic lift. It requires the coordination of various measures such as drag reduction and power increase to cross the peak. Meanwhile, the resistance on Flanks shows a steady upward trend with the change of speed.

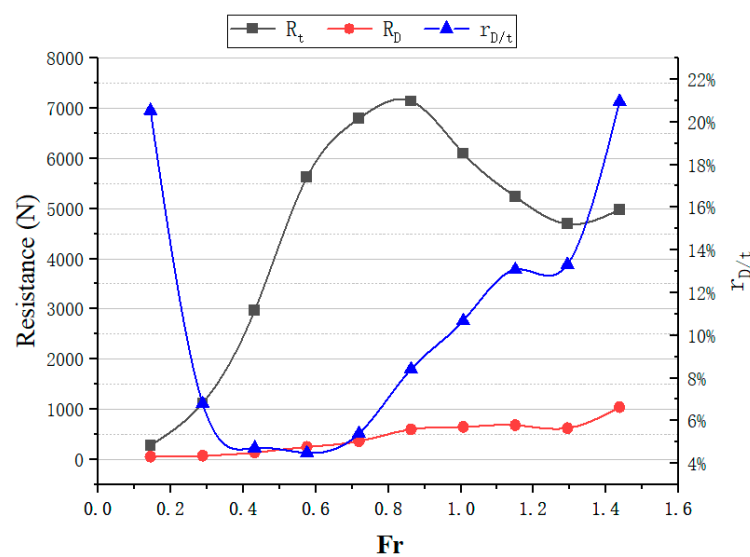


Figure 12. Flanks resistance, total resistance, and ratio  $r_{D/t}$ .

The dynamic resistance ratio  $r_{D/t}$  has large values at low speed ( $Fr < 0.3$ ) and high speed ( $Fr > 1.0$ ). It reveals the great potential for drag reduction in these two stages. In the low-speed stage, the total resistance is too small to get a significant drag reduction effect. Therefore, the drag reduction measures should be focused on the high-speed stage when Flanks can play a critical role.

### 4.3. Influence on Sailing Attitude

Previously, the contribution of the Flanks lift to the reduction of HSAV displacement has been analyzed. Furthermore, it should be noted that the lift on Flanks will also produce a trim torque, which will change the HSAV cruising attitude and affect its resistance.

Figure 13 shows the lift on Flanks and its ratio ( $r_{l/G}$ ) to the HSAV gravity under different Froude numbers.

$$r_{l/G} = F_{lD} / G \tag{13}$$

where  $F_{lD}$  shows the lift force on Flanks, and  $G$  is the vehicle’s gravity.

The contribution of Flanks to the reduction of draught is reflected by  $r_{l/G}$ . The friction resistance will be effectively reduced with the draught decrease, which can also restrain the wave to a certain extent. As shown in Figure 13, with the increase of cruising speed, the effect of Flanks improves gradually. In the transition stage, the value of  $r_{l/G}$  is maintained at about 3%, and the vehicle body is raised effectively to enter the planing condition smoothly. When the HSAV reaches the planing condition, the value of  $r_{l/G}$  rises rapidly, reaching 5.44% in  $Fr = 1.42$ .

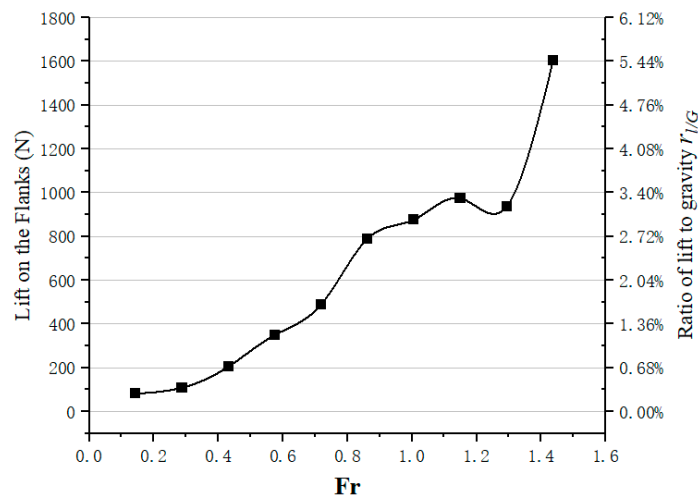


Figure 13. Lift force and lift-to-gravity ratio.

Heave and trim will also affect HSAV sailing resistance to a great extent. Increasing heave can lessen the wet area, thus lowering its resistance. Increasing the trim will enlarge the inflow angle and produce more severe waves. Figure 14 shows the effects of Flanks on heave and trim in a series of  $Fr$ . In Figure 14a, the lift will gradually replace part of buoyancy with the speed increase, hence the displacement decrease. At medium and high speeds, Flanks can significantly improve the heave, and the best effect appears at  $Fr = 1.0$ . Figure 14b shows the effect of the Flanks on reducing the maximum trim angle, which also occurred at  $Fr = 1.0$ . Thus, Flanks can obtain the best heave and trim effect when  $Fr = 1.0$  with a  $30^\circ$  installation angle.

Figure 15 shows the cruising attitude and waveform when Froude numbers are 0.72, 0.86, and 1.0. The diagram helps to clarify better the attitude change of HSAV and Flanks' effects in the transition stage. When  $Fr = 0.72$ , Flanks significantly raise the vehicle gravity center, and the bow is raised out of the water. With the increase of speed, the influence of bow wave declines, and the wave caused by grooves become more critical. The installation of Flanks makes this conversion process faster.

When  $Fr = 0.86$ , the bow has left the water and trim reached maximum, one of the reasons for the resistance peak. In this stage, Flanks play a specific role in alleviating the water intake into the groove but minor on the attitude. When  $Fr = 1.0$ , the cruising attitude begins to stabilize, and the vehicle gradually enters the planing condition. The wave around the Flanks gets sharp, but the trim and the viscous pressure resistance are reduced.

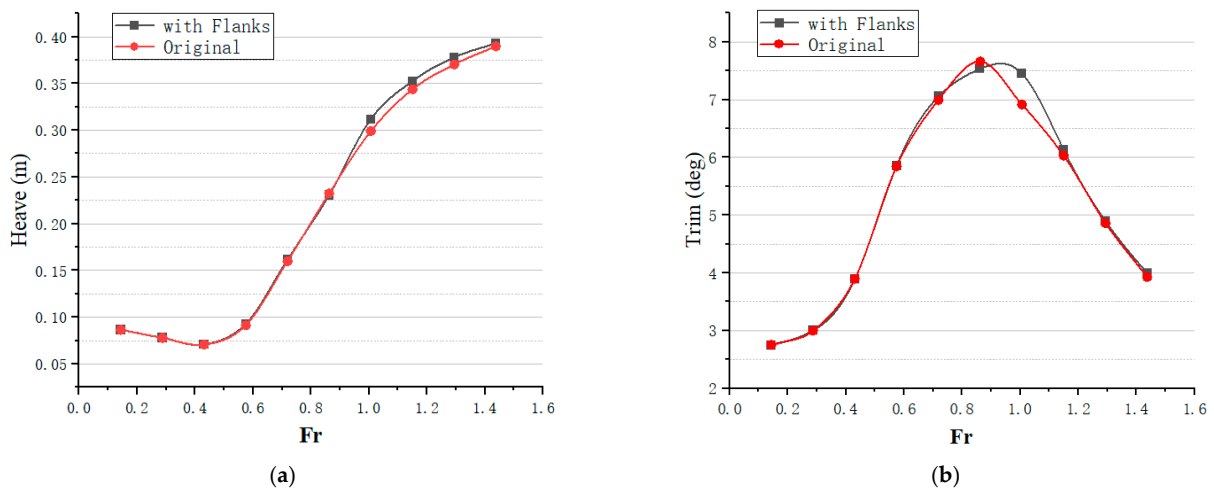
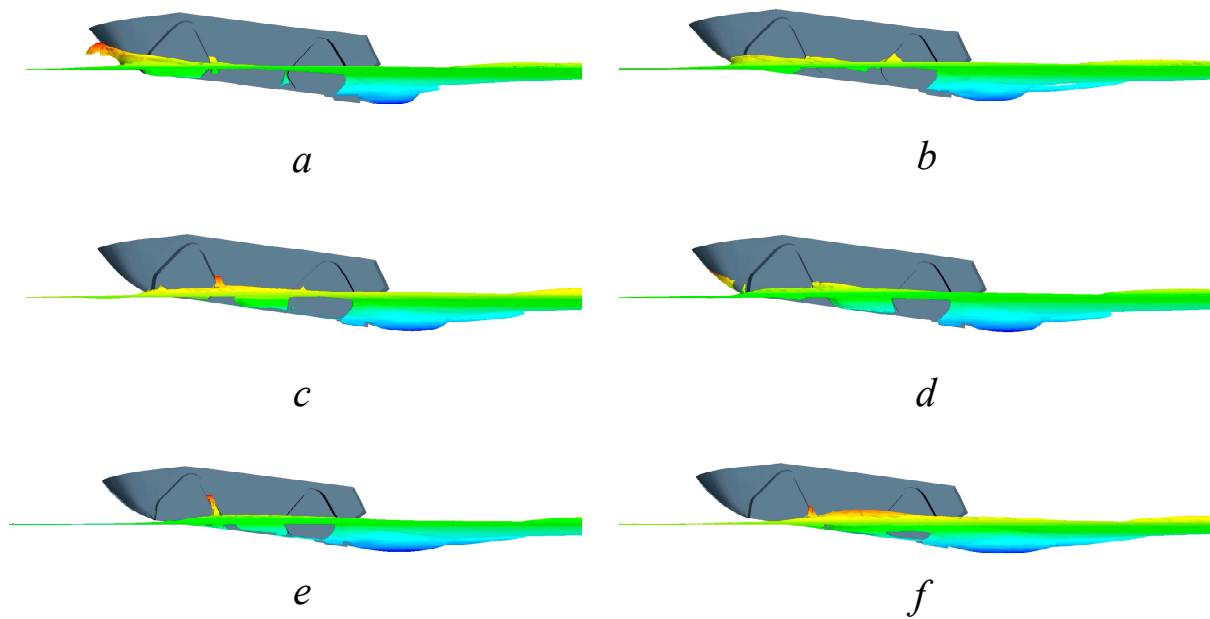


Figure 14. Comparison of Heave and Trim of the two schemes. (a) Heave, (b) Trim.



**Figure 15.** Sailing stage of HSAV at different Froude numbers ((a)  $Fr = 0.72$ , Original; (b)  $Fr = 0.72$ , Flanks; (c)  $Fr = 0.86$ , Original; (d)  $Fr = 0.86$ , Flanks; (e)  $Fr = 1.0$ , Original; (f)  $Fr = 1.0$ , Flanks).

4.4. Influence on Resistance Composition

According to the double body test description in Section 2, the composition of resistance was solved by CFD. From Formulas (5) and (6), the calculation formula of  $(1 + k)$  can be obtained as  $1 + k = C_{t'} / C_{f'}$ , where  $C_{t'}$  and  $C_{f'}$  can be calculated by CFD. Table 6 shows values of  $(1 + k)$  under different Froude numbers, where G0 represents the original vehicle and G1 represents the vehicle with Flanks.

**Table 6.**  $(1 + k)$  of HSAV with or without Flanks at different Froude numbers.

<i>Fr</i>	0.14	0.29	0.43	0.57	0.72	0.86	1.01	1.15	1.29	1.44
$(1 + k), G0$	14.33	12.70	16.83	22.59	22.34	25.72	23.35	20.43	16.56	16.19
$(1 + k), G1$	14.42	15.35	17.48	22.23	23.75	25.67	23.92	20.51	16.68	15.87

The three-dimensional method was used to deal with the results. The total and friction resistance can be calculated directly by CFD software, the viscous pressure and wave-making resistance can be calculated according to the Equation (5).

The resistance composition of a HSAV without and with Flanks is shown in Figure 16. It can be seen from the figure that the proportion of friction resistance is small, which is only 3–5% (Figure 16b). With the increase of speed, the friction resistance increases at first and then decreases (Figure 16a). This trend is caused by the decrease in heave and wet areas. Due to the small proportion of friction resistance, the effect of Flanks is not significant, but it can still be seen that the best effect occurs in  $Fr = 1.0$ .

The viscous pressure resistance increases sharply at low speed until it reaches the maximum at about  $Fr = 0.86$ , then decreases. Flanks accelerate this trend, advancing the peak of viscous pressure resistance and making the decline curve steeper. At  $Fr = 1.0$ , Flanks significantly reduced the proportion of viscous pressure from 4700 to 3200 N by about 32%. In the meantime, Flanks can obtain the best heave and trim effect when  $Fr = 1.0$ , as shown in Figure 14. The viscous pressure resistance accounts for the largest component of resistance when  $Fr < 1.2$ , but the wave-making resistance gradually surpasses it since the HSAV enters the planing condition.

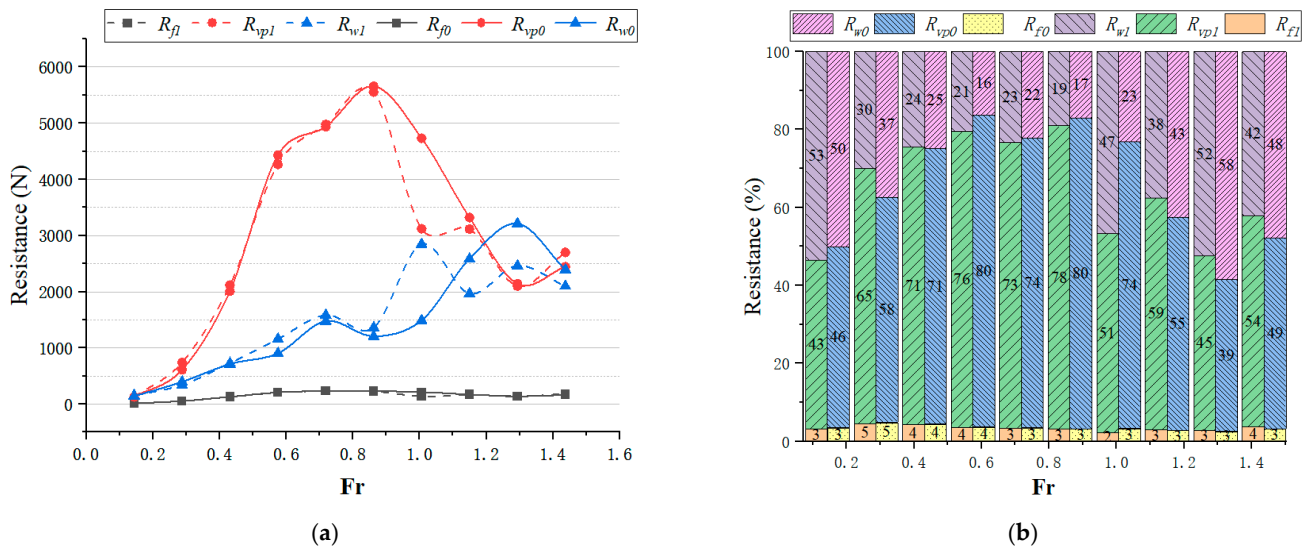


**Figure 16.** Resistance with and without Flanks at different Froude numbers (solid line and subscript 0—Origin; dotted line and subscript 1—Flanks). (a) Resistance composition, (b) proportion of composition.

The wave-making resistance of the original vehicle model raises with the increase of speed, reaching the peak value at about  $Fr = 1.3$ . In the meantime, the wave-making resistance becomes the largest source of water resistance. Flanks advance the peak of the wave-making resistance at  $Fr = 1.0$  and effectively lower the number in the planing condition.

The side wave of the HSAV can explain the reduction of wave-making resistance. The influence of Flanks on the side wave in the planing condition is shown in Figure 17. The airfoil areas on both sides of the vehicle are mainly caused by waves at concave grooves. Compared with Figure 17a, the diffusion range and wave height in Figure 17b are lower. It proves that Flanks can effectively weaken the wave at grooves and reduce related resistance.

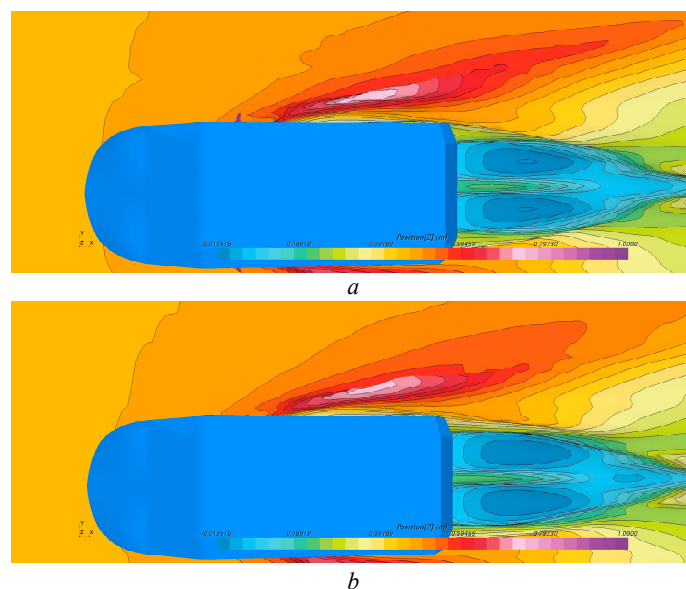


**Figure 17.** Wake flow on both sides of HSAV with or without Flanks in planing condition ((a) origin, (b) Flanks).

### 5. Model Test

As the principal measure of resistance prediction and performance analysis, the test method is still widely used in researching and designing an amphibious vehicle [42–44]. Towing test has high precision and reliable experiment results. Nevertheless, it is necessary

to make the ship model and carry out experiments in a professional pool, with time-consuming and high cost, hence is not suitable for frequent tests and modifications. After careful consideration of the cost, time, and precision, a vehicle model self-navigation experiment was adopted. In previous parts, the effect of the Flanks was analyzed by CFD, and the accuracy was verified by the towing test. Therefore, there was no need to verify the previous data again. In this part, a new method was explored to analyze the impact of configuration changes qualitatively.

### 5.1. Test Platform

3D printing technology was adopted to make the integrated HSAV model, designed with a ratio of 1:10 to the actual vehicle. A jet pump was adopted to drive forward. The power system consists of batteries, motors, jet pumps, and steering gear. As shown in Figure 18, the power system was arranged separated. The integrated power system can make a free fore and aft movement relatively through the slideway on the inner wall of the vehicle. In this way, the freedom along the longitudinal direction is released. The thrust acted on the vehicle can be measured by force sensors between the vehicle and the power system. When the HSAV travels at a constant speed, the thrust can be regarded as equal to the resistance of the vehicle, on the premise that the friction generated by the slide is negligible.

The test model was equipped with a flight controller and GPS. GPS was used to measure the vehicle's speed, and the flight controller collects GPS signals. The data transmission station was connected with the remote ground station, and the data collection and analysis can be carried on the ground station. Data collected by the force sensor was converted by the digital transmitter and stored in the offline data storage module. The data storage module was adjusted to the same time signal of the flight controller, so the velocity and force of the test model can be matched. Parameters of these instruments are shown in Table 7.

Figure 19 shows the picture of the experiment structure. The shell was hollow, and the mass was less than 1.5 kg. The weight of the power system and the battery was nearly 1.2 kg, and other instruments were less than 0.5 kg. The location of the battery can be moved to adjust the center of gravity. The critical purpose of weight control is to ensure that Flanks are located near the water surface so that the actual performance of the Flanks can be verified.

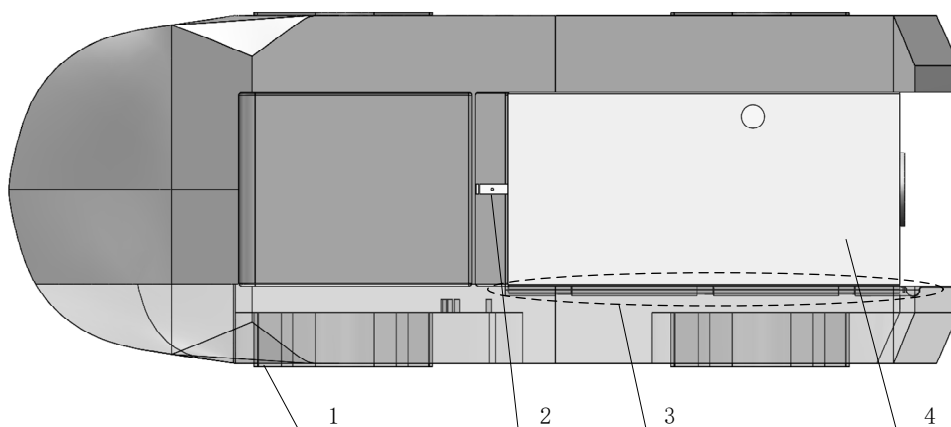


**Figure 18.** Diagram of test model structure. 1—car body; 2—sensor; 3—slideway; 4—power system.

**Table 7.** Parameters of model test instruments.

Instrument	Parameter	Instrument	Parameter
Flight controller	Pixhawk V1.4.1	Jet propeller	40 mm calibers (plastic)
GPS	M8N	Battery	25C 4000 mAh
Force sensor	JLBS-MD	Motor	3674 brushless motor

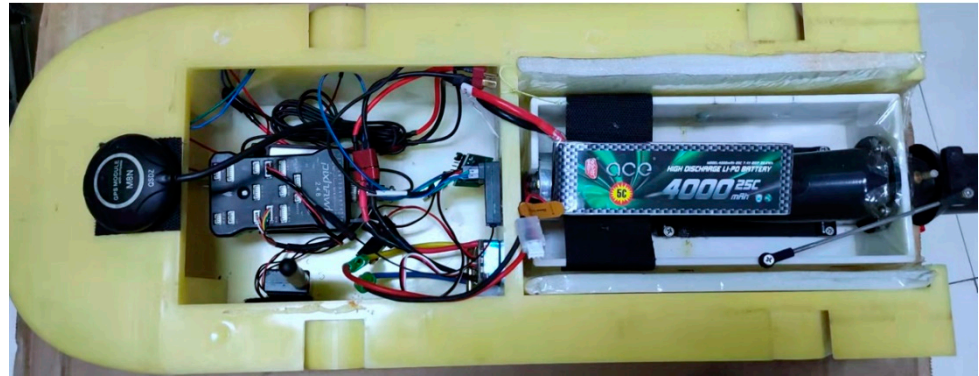


**Figure 19.** Picture of the experiment structure.

5.2. Test Design

The self-propulsion test of the HSAV was carried out in a pond without running water (the dotted line area in Figure 20). Since the pond had independent water flow with no upstream and downstream, the water surface was calm in windless weather and met the requirement of a static water test.

The experiment was carried out on a sunny, windless day with calm water. The scheduled track was from point A to B (Figure 20), and the motor of the jet pump was guaranteed to be in the same power gear in each test. Without and with Flanks, multiple tests at different speeds were carried out. The velocity and resistance were extracted from the experiment data after the speed was stabilized.



**Figure 20.** Diagram of the experiment site.

5.3. Data Verification

A series of data points were measured in the experiment, and the total resistance coefficient was plotted, as shown in Figure 21. Due to the uncontrollable errors in model machining and test (such as machining accuracy, natural waves, etc.), the volume Froude number with better tolerance for shape and waterline was selected [13].



Figure 21 shows that Flanks have a noticeable drag reduction effect at medium and high speeds. With a slight trim and high waterline at low speed, Flanks will increase the total resistance to a certain extent. Consequently, the drag reduction effect of Flanks is essentially related to the waterline and trim angle. Moreover, when the HSAV sails with different trim angles, the optimal angle of Flanks should also be changed accordingly.

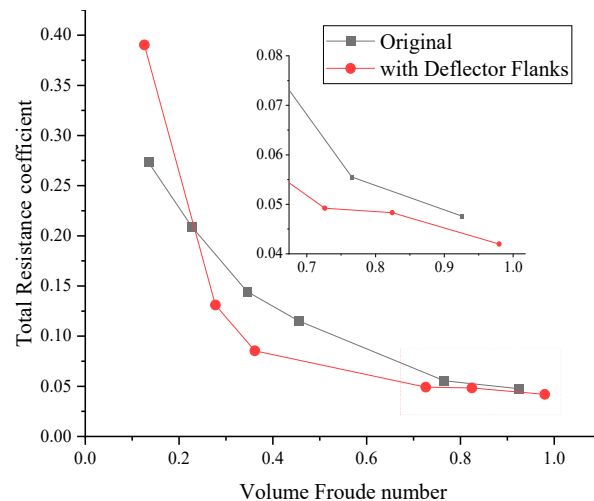


Figure 21. Diagram of test data.

## 6. Conclusions

In this paper, a drag reduction device of a HSAV was presented, which was mainly designed to solve the problem of sizeable additional resistance at concave grooves. Moreover, Flanks have easy installation and operation.

The drag reduction effects and the principle of Flanks were discussed in detail through theoretical analysis and numerical calculations. The CFD method combined with a self-propelled test was used to verify the drag reduction effect of Flanks. Results show that the Flanks have an excellent drag reduction effect at medium and high speed, which can weaken the viscous pressure resistance and wave-making resistance. The conclusions can be summarized as follows:

- (a) Flanks mainly affect the friction resistance by reducing the wet area and changing the direction of the tangential force on concave grooves. Additionally, the former one is more significant. However, considering that its proportion is less than 5%, the influence of friction resistance is not decisive. In addition, the viscous pressure resistance and wave-making resistance occupy a large proportion, which is related to the concave groove cavity and vehicle's attitude. Flanks can effectively influence the wave-making resistance and viscous pressure resistance at the concave groove by improving the inflow angle and reducing the wave height. Moreover, the resistance can be indirectly affected by Flanks in changing the attitude of the vehicle body.
- (b) Flanks have a good effect on increasing HSAV sinkage, especially at medium and high speeds. After the installation of Flanks, the trim angle in the transition stage is changed, which has an active influence on the resistance peak.
- (c) Flanks begin to exert an overall drag reduction effect when  $Fr > 1.0$ . With a fixed installation angle of  $30^\circ$ , the drag reduction effect will reach a maximum of 16% at  $Fr = 1.23$ . Therefore, Flanks ought to be folded at low speed and unfolded at high speed. Furthermore, the Flanks angle should be dynamically adjusted according to the velocity and attitude of the HSAV to achieve the best drag reduction effect.
- (d) The double-body test was used to analyze the resistance composition of the HSAV. Results show that Flanks accelerate the decrease of viscous pressure resistance and effectively reduce the wave-making resistance in the planing condition.

- (e) A self-propulsion test was used to verify the drag reduction effect of Flanks. Different from the CFD method, this test was only used to analyze the influence qualitatively. Results show that Flanks have a certain drag reduction ability at high speed.

In this paper, the drag reduction effect of Flanks was studied, and the principle was analyzed. In the subsequent study, the parameters of the Flank will be further adjusted and studied to improve its effectiveness.

**Author Contributions:** Data curation, B.L.; methodology, X.X.; writing—original draft, D.P.; writing—review and editing, D.P. All authors have read and agreed to the published version of the manuscript.

**Funding:** This research received no external funding.

**Acknowledgments:** The authors wish to thank Bolong Liu for useful and interesting discussions on the subject.

**Conflicts of Interest:** The authors declare that they have no known competing financial interest or personal relationships that could have appeared to influence the work reported in this paper.

## References

- Ehrlich, I.R.; Kamm, I.O.; Worden, G. Water performance of amphibious vehicles. Part 1—Drag and water speed: Part I—Drag and water speeds. *J. Terramech.* **1970**, *7*, 61–102. [[CrossRef](#)]
- Duan, L.; Yao, K.; Pan, X.; Hou, Z.; Tian, X. Study on force characteristics and resistance for water by amphibious vehicle. In Proceedings of the International Conference on Mechanical Engineering & Intelligent Systems, San Fransisco, CA, USA, 21–23 October 2015.
- Latorre, R.; Arana, J. Reduction of amphibious vehicle resistance and bow swamping by fitting a wave cancellation bow plate. *Naval Eng. J.* **2011**, *123*, 81–89. [[CrossRef](#)]
- Ehrlich, I.R.; Kamm, I.O.; Worden, G. *Studies of off-Road Vehicles in the Riverine Environment. Volume I. Performance Afloat*; AD0688965; 1969/01/01/; Stevens Inst of Tech Hoboken NJ Davidson Lab.: Hoboken, NJ, USA, 1969; p. 66.
- Jingtao, Z.; Huaiguang, W.; Liang, Z. The flow field simulation and resistance component analysis of amphibious vehicle based on CFD. *Ship Sci. Technol.* **2013**, *35*, 139–143. [[CrossRef](#)]
- Tao, W.; Guoying, X.; Xinmin, Y.; Jingtao, Z. Numerical simulation of two phases flow field around amphibious vehicle and analysis of power performance on water. *Chin. J. Mech. Eng.* **2008**, *44*, 168–172.
- Lee, S.-J.; Lee, T.-i.; Lee, J.-J.; Nam, W.; Suh, J.-C. Hydrodynamic characteristics of a hydrofoil-assisted amphibious vehicle. *J. Ship Res.* **2017**, *61*, 15–22. [[CrossRef](#)]
- Bratan, S.; Abdulov, S.; Trusevich, I.; Volkov, A.; Gorbatyuk, S.; Leonov, S.; Roshchupkin, S. Ensuring the amphibious capabilities of the amphibious vehicle based on the hydrodynamic buoyancy principle. *MATEC Web Conf.* **2018**, *224*. [[CrossRef](#)]
- Abd Rahman, N.A.; Malik, A.M.A.; Nakisa, M.; Abd Rahman, N.; Manap, N. Numerical prediction on resistance reduction of multi-purpose amphibious vehicle (MAV) due to air-cushion effect in a regular wave. *J. Phys. Conf. Ser.* **2020**, *1432*. [[CrossRef](#)]
- Nakisa, M.; Maimu, A.; Ahmed, Y.M.; Behrouzi, F.; Tarmizi, A. Numerical estimation of shallow water effect on multipurpose amphibious vehicle resistance. *J. Naval Archit. Mar. Eng.* **2017**, *14*, 1–8. [[CrossRef](#)]
- Helvacioğlu, S.; Helvacioğlu, I.H.; Tuncer, B. Improving the river crossing capability of an amphibious vehicle. *Ocean Eng.* **2011**, *38*, 2201–2207. [[CrossRef](#)]
- Sun, C.; Xu, X.; Wang, W.; Xu, H. Influence on stern flaps in resistance performance of a caterpillar track amphibious vehicle. *IEEE Access* **2020**, *8*, 123828–123840. [[CrossRef](#)]
- Sheng, Z.; Liu, Y. *Principles of Ships*; Shanghai Jiaotong University Press: Shanghai, China, 2005; Volume 1.
- Zou, J.; Lu, S.; Jiang, Y.; Sun, H.; Li, Z. Experimental and numerical research on the influence of stern flap mounting angle on double-stepped planing hull hydrodynamic performance. *J. Mar. Sci. Eng.* **2019**, *7*, 346. [[CrossRef](#)]
- Park, D.-M.; Lee, J.-H.; Jung, Y.-W.; Lee, J.; Kim, Y.; Gerhardt, F. Experimental and numerical studies on added resistance of ship in oblique sea conditions. *Ocean Eng.* **2019**, *186*, 106070. [[CrossRef](#)]
- Ohring, S. Three-dimensional ship wave generation using an efficient finite difference scheme with double model linearization. *J. Comput. Phys.* **1981**, *41*, 89–114. [[CrossRef](#)]
- Abbasnia, A.; Guedes Soares, C. Fully nonlinear and linear ship waves modelling using the potential numerical towing tank and NURBS. *Eng. Anal. Bound. Elem.* **2019**, *103*, 137–144. [[CrossRef](#)]
- Raven, H.C.; Van der Ploeg, A.; Starke, A.; Eça, L. Towards a CFD-based prediction of ship performance—progress in predicting full-scale resistance and scale effects. *In. J. Mar. Eng.* **2008**, *150*, A4.
- Terziev, M.; Tezdogan, T.; Incecik, A. A geosim analysis of ship resistance decomposition and scale effects with the aid of CFD. *Appl. Ocean Res.* **2019**, *92*, 101930. [[CrossRef](#)]
- Wang, Z.-Z.; Xiong, Y.; Wang, R.; Shen, X.-R.; Zhong, C.-H. Numerical study on scale effect of nominal wake of single screw ship. *Ocean Eng.* **2015**, *104*, 437–451. [[CrossRef](#)]

21. Islam, H.; Guedes Soares, C. Effect of trim on container ship resistance at different ship speeds and drafts. *Ocean Eng.* **2019**, *183*, 106–115. [[CrossRef](#)]
22. Inverno, J.; Neves, M.G.; Didier, E.; Lara, J.L. Numerical simulation of wave interacting with a submerged cylinder using a 2D RANS model. *J. Hydro-Environ. Res.* **2016**, *12*, 1–15. [[CrossRef](#)]
23. Voet, L.J.A.; Ahlfeld, R.; Gaymann, A.; Laizet, S.; Montomoli, F. A hybrid approach combining DNS and RANS simulations to quantify uncertainties in turbulence modelling. *Appl. Math. Model.* **2021**, *89*, 885–906. [[CrossRef](#)]
24. Xiaowei, W.; Tao, W.; Xinmin, Y. Study on turbulence models for simulation on flow field around tracked amphibious vehicle. *Comput. Simul.* **2012**, *29*, 10–14.
25. Spalart, P.; Allmaras, S. A one-equation turbulence model for aerodynamic flows. *AIAA* **1992**, *439*, 1–22. [[CrossRef](#)]
26. Ghadimi, P.; Dashtimanesh, A.; Chekab, M.A.F. Introducing a new flap form to reduce the transom waves using a 3-D numerical analysis. *Int. J. Comput. Sci. Eng.* **2016**, *12*, 265–275. [[CrossRef](#)]
27. Launde, B.E.; Spalding, D.B. *Lectures in Mathematical Models of Turbulence*; Cambridge University Press: Cambridge, UK, 1973; Volume 57, pp. 826–828.
28. Yakhot, V.; Orszag, S.A. Renormalization group analysis of turbulence. I. Basic theory. *J. Sci. Comput.* **1986**, *1*, 3–51. [[CrossRef](#)]
29. Yang, Z.; Shih, T.H.; Shabbir, A.; Zhu, J.; Liou, W.W. A new K-epsilon Eddy Viscosity model for high reynolds number turbulent flows: Model development and validation. *NASA Sti/Recon Tech. Rep. N* **1994**, *95*, 11442.
30. Menter, F.R. Two-equation eddy-viscosity turbulence models for engineering applications. *AIAA J.* **1994**, *32*, 1598–1605. [[CrossRef](#)]
31. Voloshin, V.; Chen, Y.K.; Calay, R.K. A comparison of turbulence models in airship steady-state CFD simulations. *arXiv Prepr.* **2012**, arXiv:1210.2970.
32. Brizzolara, S.; Salian, R. Adjustable energy saving device for transom stern hulls. In Proceedings of the SNAME Maritime Convention, Providence, RI, USA, 24–27 October 2018.
33. Ozdemir, Y.H.; Barlas, B. Numerical study of ship motions and added resistance in regular incident waves of KVLCC2 model. *Int. J. Naval Archit. Ocean Eng.* **2017**, *9*, 149–159. [[CrossRef](#)]
34. Procedures, I.R. ITTC—recommended procedures-performance, propulsion 1978 ITTC performance prediction method. In Proceedings of the 22nd International Towing Tank Conference, ITTC'99, Seoul, Korea, Shanghai, China, 5–11 September 1999; p. 7.5-02.
35. Xing, T.; Stern, F. Factors of safety for Richardson extrapolation. *J. Fluids Eng.* **2010**, *132*, 061403. [[CrossRef](#)]
36. Roy, C.; Heintzelman, C.; Roberts, S. Estimation of numerical error for 3D inviscid flows on Cartesian grids. In Proceedings of the 45th AIAA aerospace sciences meeting and exhibit, Reno, Nevada, 8–11 January 2007; p. 102.
37. Wang, J.; Zou, L.; Wan, D. CFD simulations of free running ship under course keeping control. *Ocean Eng.* **2017**, *141*, 450–464. [[CrossRef](#)]
38. Tezdogan, T.; Demirel, Y.K.; Kellett, P.; Khorasanchi, M.; Incecik, A.; Turan, O. Full-scale unsteady RANS CFD simulations of ship behaviour and performance in head seas due to slow steaming. *Ocean Eng.* **2015**, *97*, 186–206. [[CrossRef](#)]
39. Song, K.-W.; Guo, C.-Y.; Gong, J.; Li, P.; Wang, L.-Z. Influence of interceptors, stern flaps, and their combinations on the hydrodynamic performance of a deep-vee ship. *Ocean Eng.* **2018**, *170*, 306–320. [[CrossRef](#)]
40. Sigmund, S.; el Moctar, O. Numerical and experimental investigation of added resistance of different ship types in short and long waves. *Ocean Eng.* **2018**, *147*, 51–67. [[CrossRef](#)]
41. Song, K.-W.; Guo, C.-Y.; Wang, C.; Sun, C.; Li, P.; Wang, W. Numerical analysis of the effects of stern flaps on ship resistance and propulsion performance. *Ocean Eng.* **2019**, *193*, 106621. [[CrossRef](#)]
42. Demirel, Y.K.; Khorasanchi, M.; Turan, O.; Incecik, A.; Schultz, M.P. A CFD model for the frictional resistance prediction of antifouling coatings. *Ocean Eng.* **2014**, *89*, 21–31. [[CrossRef](#)]
43. Behara, S.; Arnold, A.; Martin, J.E.; Harwood, C.M.; Carrica, P.M. Experimental and computational study of operation of an amphibious craft in calm water. *Ocean Eng.* **2020**, *209*, 107460. [[CrossRef](#)]
44. Marquardt, J.G.; Alvarez, J.; von Ellenrieder, K.D. Characterization and system identification of an unmanned amphibious tracked vehicle. *IEEE J. Ocean. Eng.* **2014**, *39*, 641–661. [[CrossRef](#)]